REGION-AWARE INSTANCE CONSISTENCY LEARNING FOR APEX-FREE MICRO-EXPRESSION RECOGNITION

Anonymous authors
Paper under double-blind review

ABSTRACT

Micro-expression Recognition (MER) is challenging due to the subtle motion. Existing methods heavily rely on the onset/apex pair to capture the most discriminative motion clues. This paradigm struggles with labor-intensive apex annotation and effective utilization of data. In this paper, we propose a novel apex-free paradigm for MER that eliminates the need for expensive apex annotations while effectively capturing subtle motion dynamics. Our key insight is that frames within the sequence exhibit spatially consistent and intensity varied motion cues relative to the onset frame. Motivated by this, our method treats each sequence as a set of multiple onset/near-median motion instances. To fully exploit weaker motion information conveyed by these diverse instances, our framework introduces an Instance Region Consistency (IRC) module that enforces visual attention consistency on similar facial activation regions across different instances within the same set. Furthermore, we present a Multi-Region Discovery (MRD) module with self-supervised learning to expand attention on more subtle activation regions which are typically neglected. Extensive experiments on four public micro-expression datasets demonstrate that our proposed approach surpasses state-of-the-art methods without using any apex frame annotations.

1 INTRODUCTION

Micro-expressions (MEs) are transient and involuntary facial movements reflecting genuine emotions that individuals attempt to conceal (Ben et al., 2021). Owing to this property, the ME recognition (MER) task has demonstrated crucial potential in various applications, e.g., lie detection (O'sullivan et al., 2009) and mental health assessment (Endres & Laidlaw, 2009). Despite recent progress, MER remains challenging since MEs cover facial activation regions with imperceptible intensity and brief duration.

Existing MER methods typically regard the motion between the onset and apex frames as the fundamental cue of representing subtle ME movements. The motion is commonly estimated using optical flow or deep learning-based methods, followed by a well-designed classification model that maps the input motion to emotion labels. Although the apex frame captures the most obvious motion cues for classification, accurately identifying the apex frame requires human coders to scan the ME sequence frame-by-frame manually, which is time-consuming and demands expert knowledge. Moreover, due to the difficulty in collecting and annotating ME data, the amount of data in current ME datasets is relatively small. Therefore, relying solely on onset/apex pairs not only limits practical usage of ME data, but also increases the risk of overfitting to specific facial activation regions. While recent self-supervised methods like AVF-MAE++ (Wu et al., 2025) have been proposed to learn general facial representation to mitigate overfitting, they typically require pre-training on external large-scale datasets, incurring substantial computational costs. Therefore, learning robust and general representations directly from small-scale ME datasets remains an open and challenging problem.

In this paper, we rethink the necessity of apex frames and propose an apex-free paradigm with Region-aware Instance Consistency Learning (Ra-ICL) for MER. Our empirical observations reveal that the effective motion information is not exclusively contained in the apex frame. As shown in Figure 1, we find that frames within the sequence exhibit motion patterns that share consistent spatial activation regions compared to the onset frame, while the motion intensity across these activation regions varies over time. This combination of spatial stability and intensity variation motivates us to treat alternative pairs (e.g., onset vs. near-median) as carriers of weaker yet valid motion cues. Specifically, we propose to form instance sets composed of multiple motion instances from onset/near-median pairs for each sequence, rather than only one onset/apex pair.

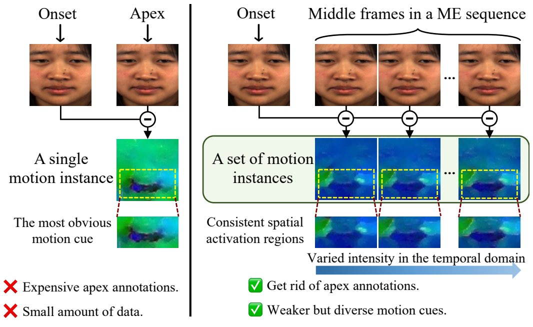
Onset
Apex
Onset
Middle frames in a ME sequence
A single motion instance
The most obvious motion cue
A set of motion instances
Consistent spatial activation regions
Varied intensity in the temporal domain
✗ Expensive apex annotations.
✗ Small amount of data.
✓ Get rid of apex annotations.
✓ Weaker but diverse motion cues.

(a) Previous methods

(b) Our observation

Figure 1: A ME sequence can be treated as a set of motion instances from multiple onset/near-median frame pairs without apex annotations. These instances exhibit consistent spatial activation regions with weaker but diverse motion cues.

To leverage diverse but weaker motion information delivered by these instances, we introduce an Instance Region Consistency (IRC) module to effectively capture subtle motion dynamics. This module is built on the observation that instances within the same set share the same emotion label and tend to activate similar facial activation regions. We randomly sample two instances to form a positive pair for each sequence and feed them through a Siamese network, obtaining their respective attention heatmaps via class activation mapping (Zhou et al., 2016). We then enforce visual attention consistency (Guo et al., 2019) between the two attention heatmaps to encourage the model to focus on similar facial activation regions across different instances. Due to the inherently low activation intensity of certain regions in MEs, attention heatmaps are prone to focus on prominent areas and neglect these subtle yet important regions. To address this issue, we further propose a Multi-Region Discovery (MRD) module inspired by recent advances in self-supervised facial representation learning (Gao & Patras, 2024). The MRD module uses a set of learnable facial queries to discover more subtle but meaningful facial regions in a self-supervised manner. Consequently, the attention of the model is expanded to encompass more subtle motion patterns.

To summarize, our main contributions are as follows:

- We rethink the necessity of apex frames and propose a novel framework Ra-ICL for apex-free MER. The ME sequence is represented by a set of multiple motion instances instead of a single onset/apex motion instance.
- We propose an IRC module to effectively capture subtle motion cues by enforcing visual attention consistency across different motion instances from the same set.
- To further enhance the perception of subtle activation regions, we present a MRD module to discover more meaningful facial regions with self-supervised learning, preventing decisions from localized activation regions.
- Extensive experiments on four public ME datasets demonstrate the effectiveness of the proposed method.

2 Related Works

Motion Features for Micro-expressions. In early works for MER, several texture-based feature descriptors were carefully designed to extract spatio-temporal features of ME motion, including LBP-TOP (Zhao & Pietikainen, 2007), HOG (Li et al., 2017), etc. Recently, researchers have adopted optical flow to characterize subtle facial muscle deformation of MEs. Optical flow serves as a robust representation of pixel-level inter-frame motion, effectively capturing both the magnitude and direction of motion. Some variants of optical flow were further proposed to offer more effective and robust motion features, such as MDMO (Liu et al., 2015) and Bi-WOOF (Liong et al., 2018). Since the apex frame reaches the maximum intensity of the ME motion, the optical flow between the onset and apex frames was typically utilized to represent observable ME motion features.

Deep Networks for Micro-expression Recognition. Existing methods typically leverage deep neural networks to extract emotion-relevant information from motion features between onset and apex frames. OFF-ApexNet (Gan et al., 2019) and Dual-Inception (Zhou et al., 2019) fed horizontal and vertical optical flow into a two-stream convolutional neural network (CNN) for feature enhancement, while STSTNet (Liong et al., 2019) further computed optical strain to form the triple

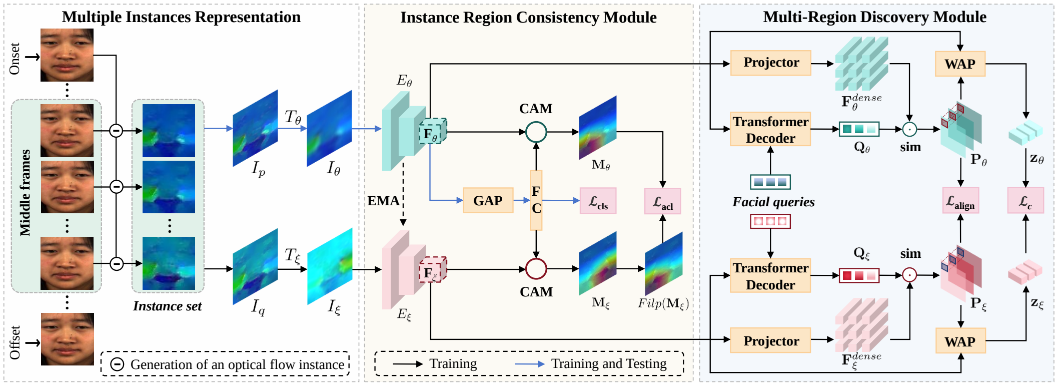

Figure 2: The framework of the proposed Ra-ICL. Given an input sequence, we generates multiple optical flow instances to form an instance set using onset/near-median frame pairs. The Instance Region Consistency (IRC) module takes random instance pairs from the instance set as input to learn effective motion information from weak yet valid motion cues, which enforces attention consistency on similar activation regions. A Multi-Region Discovery (MRD) module is further utilized to discover meaningful facial regions in a self-supervised manner, thus enhancing perception on subtle activation regions. Note that some intermediate results in MRD are omitted for brevity.

stream of a shallow 3D-CNN. In addition to CNN-based methods, Zhang et al. (2022a) first proposed a purely Transformer-based (Vaswani et al., 2017) framework SLSTT that composed of a Vision Transformer (Dosovitskiy et al., 2020) and a LSTM. Furthermore, MFDAN (Cai et al., 2024) introduced an additional RGB branch to construct a two-stream network (Simonyan & Zisserman, 2014), collaboratively modeling spatio-temporal features to enhance feature representation learning. Although these methods have achieved promising progress, they still rely on costly apex annotations to extract effective motion clues, which limits the effective utilization of ME data. To address this issue, we treat a ME sequence as a set of onset/near-median motion instances, which eliminates the need for apex annotations.

Self-supervision for Micro-expression Recognition. To alleviate data scarcity in ME research, numerous studies adopted external knowledge to improve the performance of MER models by self-supervised pre-training. SelfME (Fan et al., 2023) and SODA4MER (Zhang et al., 2025a) finetuned a first order motion model (Siarohin et al., 2019) pre-trained on the VoxCeleb dataset (Nagrani et al., 2017) to achieve self-supervised motion learning. Since the release of the large-scale ME dataset CAS(ME)^3 (Li et al., 2022), some studies have applied additional ME frames or depth information to construct self-supervised learning models. Nguyen et al. (Nguyen et al., 2023) proposed Micron-BERT, which is pre-trained on CAS(ME)^3 with specially designed modules to detect micro-movements. Li et al. (Li et al., 2025) adopted RGB and depth modalities for self-supervised contrastive pre-training, followed by fine-tuning on downstream MER tasks. Unlike these works, FRL-DGT (Zhai et al., 2023) introduced a displacement generation module that samples sufficient additional random frame pairs from the dataset to train the model in a self-supervised manner, thereby avoiding reliance on additional datasets. Similar to FRL-DGT, we do not rely on additional datasets but instead sample sufficient random instance pairs from data augmentation caused by the multiple instances representation. Through joint training of IRC and MRD modules, our method enforces the model to focus on subtle facial activation regions with diverse instance pairs as input.

3 Proposed Method

The framework of the proposed Ra-ICL is illustrated in Figure 2. Ra-ICL consists of three parts, i.e., Multiple Instances Representation (MIR), Instance Region Consistency (IRC) module, and Multi-Region Discovery (MRD) module. The MIR provides motion features for each ME sequence in the form of optical flow instance sets. The IRC module then takes random instance pairs as input to extract subtle motion information by enforcing attention consistency between instance pairs. Meanwhile, the MRD module uses a set of facial queries to discover meaningful facial regions, which constrains the attention on more activation regions with low intensity.

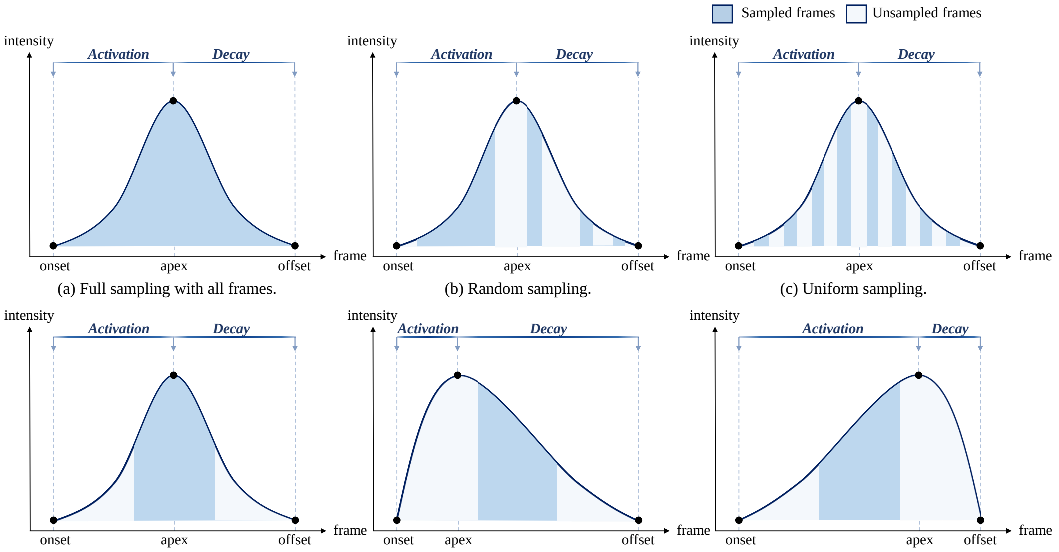

(a) Full sampling with all frames.

(b) Random sampling.

(c) Uniform sampling.

(d) Middle sampling including the apex frame.

(e) Middle sampling within the decay stage.

(f) Middle sampling within the activation stage.

Figure 3: Different sampling strategies for Multiple Instances Representation.

3.1 Multiple Instances Representation

The Multiple Instances Representation (MIR) forms the foundation of Ra-ICL, avoiding the need for apex annotations and enabling data augmentation. As shown in Figure 3, a complete ME movement can be divided into two stages: activation stage from onset to apex, and decay stage from apex to offset. During this process, the approximate spatial extent of facial activation regions (i.e., action units) remains consistent across the temporal domain, differing only in intensity. Therefore, frames other than the apex frame in a ME sequence also carry valid motion information with relatively lower intensity. Without using apex frame annotations, a ME sequence can be represented as a set of optical flow instances from the onset frame to arbitrary intra-sequence frames (see Figure 3(a)). These instances share similar facial activation regions, but vary in intensity.

Considering the computational cost of optical flow, the number of sampled frames N must be limited rather than using all frames. Compared to random sampling (see Figure 3(b)) and uniform sampling (see Figure 3(c)), middle sampling avoids low-intensity frames typically located at both ends of the sequence. As shown in Figure 3(d), under ideal conditions, the middle sampling window covers the apex frame. When the apex frame falls outside the window, the entire sampling range lies either within the activation stage or the decay stage, as illustrated in Figure 3(e)(f). In such cases, although frames with higher motion intensity are not captured, it avoids sampling frames near the sequence boundaries where the motion magnitude is close to zero. Based on the middle sampling, the amount of motion instances is expanded from a single onset/apex pair to multiple onset/near-median pairs.

For a ME sequence, we sample N consecutive frames from the middle part of the sequence. Then we obtain N optical flow feature maps using the onset and the sampled N frames by the TV-L1 method (Sánchez Pérez et al., 2013). The optical flow field O_n between the onset frame and the n-th frame can be expressed as the combination of the horizontal field u_n and the vertical field v_n:

$$O_n = \{(u_n(x,y), v_n(x,y))\}, \tag{1}$$

where $x = 1, 2, ..., H$, $y = 1, 2, ..., W$, (x, y) represents the pixel position, H and W are the height and width of the image. Moreover, following previous works (Xu et al., 2022; Cai et al., 2024), the optical strain is further combined as the third channel to form a three-dimensional tensor similar to a RGB image. Optical strain ϵ_n is defined as the first-order derivative of the optical flow field O_n. The final optical flow map $I_n \in \mathbb{R}^{H\times W\times 3}$ can be expressed as:

$$I_n = [u_n, v_n, \epsilon_n]. \tag{2}$$

3.2 Instance Region Consistency Learning

Based on MIR, we aim to learn subtle motion dynamics from motion diversity. Given a batch of ME sequences, we randomly sample two distinct optical flow instances I_p and I_q to form sufficient random instance pairs for each sequence. In this way, instances with lower intensity are systematically paired with multiple instances with higher intensity in a large pool of instance pairs. We adopt the Siamese network as BYOL (Grill et al., 2020), consisting of two branches: the online network E_θ and the target network E_ξ. Both networks have the same residual structure (He et al., 2016), but the target parameters ξ are updated with an exponential moving average (EMA) of the online parameters θ given a target decay rate $\tau \in [0, 1]$:

$$\xi = \tau\xi + (1 - \tau)\theta. \tag{3}$$

Based on spatial consistency of motion cues, the Siamese structure learns to identify invariant activation regions from diverse instance pairs. Meanwhile, activation regions with weaker motion can be effectively identified from the guidance of instances with higher intensity. Firstly, both instances I_p and I_q are fed into the online network E_θ and the target network E_ξ. We denote T_θ and T_ξ as random data transforms (e.g., color jitter and Gaussian blur) applied to E_θ and E_ξ, respectively. In the following sections, we consider the situation where I_p is processed by E_θ and I_q is processed by E_ξ. The spatial consistency requires the attention on activation regions for I_p in E_θ aligned with that of I_q in E_ξ, which can be realized by flip semantic consistency (Guo et al., 2019; Zhang et al., 2022b). Specifically, the attention region for image classification is flipped horizontally if the original image is flipped horizontally. Therefore, T_ξ performs a certain horizontal flipping on I_q.

As a result, $I_\theta = T_\theta(I_p)$ and $I_\xi = T_\xi(I_q)$ are then processed by E_θ and E_ξ separately to generate feature maps. The feature maps are extracted from the last convolutional layer, denoted as $\mathbf{F}_e \in \mathbb{R}^{C\times H\times W}$ with $e \in \{\theta, \xi\}$, where C, H, W are the number of channels, height and width of the feature map, respectively. A subsequent global average pooling (GAP) is performed on $\mathbf{F}_\theta$ and get features $f_\theta \in \mathbb{R}^{C\times 1\times 1}$. The pooled features are further resized to $f'_\theta \in \mathbb{R}^C$ and put through the fully connected (FC) layer with weights $\mathbf{W} \in \mathbb{R}^{L\times C}$ to compute the classification loss:

$$\mathcal{L}_{\text{cls}} = -\log\left(\frac{e^{\mathbf{W}_y\cdot f'_\theta}}{\sum_{j=1}^{L} e^{\mathbf{W}_j\cdot f'_\theta}}\right), \tag{4}$$

where $\mathbf{W}_y$ is the y-th weight from the FC layer, y is the given ground truth label, and L is the number of labels. Meanwhile, the attention regions of the input instance can be derived as attention heatmaps $\mathbf{M}_j(x, y) \in \mathbb{R}^{H\times W}$ by Class Activation Mapping (CAM) (Zhou et al., 2016) to indicate the relevance of spatial location (x, y) for a predicted class j. Formally, the mapping is computed through a weighted combination of feature maps over different channels:

$$\mathbf{M}_j(x, y) = \sum_{c=1}^{C} \mathbf{W}(j, c)\mathbf{F}_c(x, y), \tag{5}$$

where $\mathbf{F}_c(x, y)$ represents the activation value at spatial position (x, y) of the c-th channel, C denotes the total number of feature maps, and $\mathbf{W}(j, c)$ signifies the weight coefficient corresponding to class j for the FC layer. We compute attention heatmaps $\mathbf{M}_\theta$ and $\mathbf{M}_\xi$ for E_θ and E_ξ according to equation 5. Finally, attention consistency loss using the mean square difference is utilized to minimize the distance between $\mathbf{M}_\theta$ and $Flip(\mathbf{M}_\xi)$:

$$\mathcal{L}_{\text{acl}} = \frac{1}{LHW}\sum_{j=1}^{L} \|\mathbf{M}_{\theta j} - Flip(\mathbf{M}_{\xi j})\|_2\,, \tag{6}$$

where $\mathbf{M}_{\theta j}$ and $\mathbf{M}_{\xi j}$ indicate the attention heatmaps for I_θ and I_ξ respectively with label j. Through joint optimization of $\mathcal{L}_{\text{cls}}$ and $\mathcal{L}_{\text{acl}}$, the Siamese network learns to associate facial activation regions with corresponding emotion labels.

3.3 Self-supervised Multi-Region Discovery

The IRC module is guided to focus on facial activation regions related to emotional labels. However, for a classification model, only the most discriminative regions are recognized (Wei et al., 2017), and some weaker but important activation regions are discarded. This phenomenon leads to classification error on the ME data with high inter-class similarity. To address this issue, we present a Multi-Region Discovery (MRD) module to discover more meaningful facial regions for a comprehensive decision rather than relying on localized activation regions.

To automatically discover different facial regions, we use a set of facial queries to look up the whole image. Specifically, following MaskFormer (Cheng et al., 2021), a Transformer decoder followed by a MLP takes N facial queries (Query) that are learnable positional embeddings and the feature map $\mathbf{F}_e$ (Key and Value) as input to predict N facial mask embeddings $\mathbf{Q}_e \in \mathbb{R}^{N\times D}$. Each facial mask embedding is associated with a facial region. Then we generate N corresponding heatmaps $\mathbf{S}_e \in \mathbb{R}^{N\times H\times W}$ to locate facial regions on the feature map as:

$$\mathbf{S}_e[m,u,v] = \mathrm{sim}(\mathbf{Q}_e[m,:], \mathbf{F}_e^{dense}[*,u,v]), \tag{7}$$

where $\mathbf{F}_e^{dense} \in \mathbb{R}^{D\times H\times W}$ is the dense feature map obtained by projecting $\mathbf{F}_e$ through the projector H_e, and $\mathrm{sim}(\cdot)$ is the cosine similarity function. The m-th heatmap $\mathbf{S}_e[m,u,v]$ quantifies the relevance of the pixel (u,v) in the dense feature map $\mathbf{F}_e^{dense}$ to the m-th facial region indicated by $\mathbf{Q}_e[m,:]$. To prevent heatmaps of specific facial regions from dominating, $\mathbf{S}_e$ is normalized along the channel dimension via Softmax, resulting in a group of probabilistic heatmaps $\mathbf{P}_e \in \mathbb{R}^{N\times H\times W}$:

$$\mathbf{P}_e[m,u,v] = \frac{\exp(\mathbf{S}_e[m,u,v])}{\sum_{n=1}^{m}\exp(\mathbf{S}_e[n,u,v])}. \tag{8}$$

Each channel $\mathbf{P}_e[m,*,*] \in \mathbb{R}^{H\times W}$ represents a 2D heatmap that highlights the m-th facial region. Based on the spatial consistency of instance pairs, we formulate the heatmap learning process as a deep clustering problem (Caron et al., 2020) to provide learning signals. Specifically, we treat the N learnable facial queries as the centers of N facial region clusters. Therefore, the normalized per-pixel cluster assignment $\mathbf{P}_e[*,u,v]$ between E_θ and E_ξ should keep aligned, which is measured by the cross-entropy loss:

$$CE(\mathbf{P}_\xi[*,u,v], \mathbf{P}_\theta[*,u,v]|I_p) = -\sum_{m=1}^{N} \mathbf{P}_\xi[m,u,v]\log \mathbf{P}_\theta[m,u,v], \tag{9}$$

where the target network provides a stable target. Notice that the equation 9 is formulated for the scenario where I_p is processed by E_θ. We define the symmetric self-supervised alignment loss for both augmented instances as:

$$\mathcal{L}_{\text{align}} = \frac{1}{HW}\sum_{u,v}\Big(CE(\mathbf{P}_\xi[*,u,v], \mathbf{P}_\theta[*,u,v]|I_p) + CE(\mathbf{P}_\xi[*,u,v], \mathbf{P}_\theta[*,u,v]|I_q)\Big). \tag{10}$$

Similar to $\mathcal{L}_{\text{acl}}$, the spatial consistency of local facial regions discovered by the MRD module should be considered. Based on the learned heatmaps $\mathbf{P}_e$, the latent representations for local facial regions are obtained through:

$$\mathbf{h}_e^m = \mathbf{P}_e[m,*,*] \otimes \mathbf{F}_e = \frac{1}{\sum_{u,v}\mathbf{P}_e[m,u,v]}\sum_{u,v}\mathbf{P}_e[m,u,v]\mathbf{F}_e[*,u,v], \tag{11}$$

where $\otimes$ denotes channel-wise Weighted Average Pooling (WAP), $\mathbf{h}_e^m \in \mathbb{R}^C$ is the corresponding latent representation of the m-th facial region produced with $\mathbf{P}_e[m,*,*]$. The projector H_e is performed on these latent representations to obtain facial embeddings:

$$\mathbf{z}_e^m = H_e(\mathbf{h}_e^m). \tag{12}$$

The cosine similarity is used to measure the consistency of produced local facial regions between E_θ and E_ξ:

$$\mathrm{sim}(\mathbf{z}_\theta, \mathbf{z}_\xi|I_p) = \frac{1}{N}\sum_{m=1}^{N}\mathrm{sim}(G_\theta(\mathbf{z}_\theta^m), \mathbf{z}_\xi^m)), \tag{13}$$

where G_θ is the predictor on top of the projector H_θ. Similar to equation 10, equation 13 should be computed symmetrically for both augmented instances as:

$$\mathcal{L}_c = \mathrm{sim}(\mathbf{z}_\theta, \mathbf{z}_\xi|I_p) + \mathrm{sim}(\mathbf{z}_\theta, \mathbf{z}_\xi|I_q). \tag{14}$$

3.4 Overall Objective

We jointly optimize the equation 15:

$$\mathcal{L} = \lambda_1\mathcal{L}_{\text{cls}} + \lambda_2\mathcal{L}_{\text{acl}} + \lambda_3(\mathcal{L}_{\text{align}} + \mathcal{L}_c), \tag{15}$$

where $\lambda_1, \lambda_2, \lambda_3$ are the loss weight for balancing the classification, IRC and MRD respectively. As shown in Figure 2, both online and target networks are jointly updated during training. For inference, only the online network is utilized for classification as with BYOL (see Appendix A.1.3).

Table 1: Comparison with SOTA methods in terms of UF1(%) and UAR(%) under the CDE setting. The best results are highlighted in **bold**, while the second-best results are marked with an underline.

Methods	Composite		CASME II		SAMM		SMIC-HS	
	UF1	UAR	UF1	UAR	UF1	UAR	UF1	UAR
LBP-TOP (Zhao & Pietikainen, 2007)	58.82	57.85	70.26	74.29	39.54	41.02	20.00	52.80
Bi-WOOF (Liong et al., 2018)	62.96	62.27	78.05	80.26	52.11	51.39	57.27	58.29
STSTNet (Liong et al., 2019)	73.53	76.05	83.82	86.86	65.88	68.10	68.01	70.13
RCN (Xia et al., 2019)	74.32	71.90	85.12	81.23	76.01	67.15	63.26	64.41
FeatRef (Zhou et al., 2022)	78.38	78.32	89.15	88.73	73.72	71.55	70.11	70.83
SLSTT (Zhang et al., 2022a)	81.60	79.00	90.10	88.50	71.50	64.30	74.00	72.00
FRL-DGT (Zhai et al., 2023)	81.20	81.10	91.90	90.30	77.20	75.80	74.30	74.90
MFDAN (Cai et al., 2024)	84.53	86.88	91.34	93.26	78.71	81.96	68.15	70.43
HTNet (Wang et al., 2024)	86.03	84.75	95.32	95.16	81.31	81.24	80.49	79.05
MPFNet (Ma et al., 2025)	83.20	84.70	87.90	89.50	79.10	82.60	78.10	78.30
CSARNet (Zhao et al., 2025)	82.39	83.00	92.54	92.98	77.32	78.51	76.05	76.39
Ra-ICL (ours)	**88.05**	**89.11**	**96.20**	**96.20**	**86.68**	**88.85**	**81.79**	**82.74**

4 EXPERIMENTS

4.1 EXPERIMENTAL SETTINGS

Datasets. We conducted experiments on four public ME datasets: CASME II (Yan et al., 2014), SAMM (Davison et al., 2016), SMIC-HS (Li et al., 2013) and CAS(ME)^3 (Li et al., 2022). Appendix A.1.1 introduces the details of datasets.

Implementation Details. The framework is implemented by Pytorch (Paszke et al., 2019). Both online and target networks adopt randomly initialized ResNet18 (He et al., 2016) as the backbone with target decay rate $\tau = 0.99$. The optimizer is Adam with an initial learning rate of 0.001 and a weight decay of 0.0001. We train the framework with a batch size of 32 and exponential learning rate decay with the gamma of 0.9 for 100 epochs. For MIR, the number of sampled frames N is set to 16, which is determined by the frame rate prior. For MRD, the number of facial queries is set to 8. In equation 15, we take $\lambda_1 = \lambda_2 = \lambda_3 = 0.5$. Appendix A.1.2 introduces the details of determining the N of MIR, while Appendix A.2 provides relevant hyper-parameter analysis.

Evaluation Protocols. To evaluate the model performance on CASME II, SAMM and SMIC-HS, we adopt the Composite Database Evaluation (CDE) (See et al., 2019) with Leave-one-subject-out (LOSO) cross-validation to ensure a fair comparison. The CDE setting combines samples from CASME II, SAMM and SMIC-HS into a composite dataset for training. For the evaluation on CAS(ME)^3, 3-class, 4-class and 7-class evaluation with LOSO are reported following previous works (Li et al., 2022; Nguyen et al., 2023). More details are displayed in Appendix A.1.4.

Metrics. As per standard (See et al., 2019), we adopt the Unweighted F1-score (UF1) and Unweighted Average Recall (UAR) to assess model performance. Compared to Accuracy (Acc), UF1 and UAR provide a more balanced judgement on all classes.

Table 2: Comparison with other SOTA methods in terms of UF1 (%) and UAR (%) on the CAS(ME)^3 dataset. The best results are highlighted in **bold**, while the second-best results are marked with underline.

Methods	Classes	UF1	UAR
STSTNet (Liong et al., 2019)	3	37.95	37.92
RCN (Xia et al., 2019)	3	39.28	38.93
FeatRef (Zhou et al., 2022)	3	34.93	34.13
μ-BERT (Nguyen et al., 2023)	3	56.04	61.25
HTNet (Wang et al., 2024)	3	57.67	54.15
Lite-Point-GCN (Zhang et al., 2025b)	3	68.19	74.12
Ra-ICL (ours)	3	**75.85**	**74.54**
Baseline (Li et al., 2022)	4	29.15	29.10
Baseline(+Depth) (Li et al., 2022)	4	30.01	29.82
μ-BERT (Nguyen et al., 2023)	4	47.18	49.13
Lite-Point-GCN (Zhang et al., 2025b)	4	47.64	53.66
Ra-ICL (ours)	4	**61.03**	**58.48**
Baseline (Li et al., 2022)	7	17.59	18.01
Baseline(+Depth) (Li et al., 2022)	7	17.73	18.29
μ-BERT (Nguyen et al., 2023)	7	32.64	32.54
Lite-Point-GCN (Zhang et al., 2025b)	7	35.64	41.59
Ra-ICL (ours)	7	**44.32**	**43.17**

Table 3: Ablation study of key components of Ra-ICL. "→X" indicates replacing the corresponding component with X. The best results are **bolded**, and the second-best results are underlined.

Method	MIR	IRC	MRD	Composite		CASME II		SAMM		SMIC-HS	
				UF1	UAR	UF1	UAR	UF1	UAR	UF1	UAR
M1	→Apex*	×	×	83.22	82.64	94.78	95.73	81.43	80.39	75.13	74.40
M2	✓	×	×	84.91	83.72	93.83	93.36	83.68	82.76	78.70	77.86
M3	→Apex*	✓	✓	87.61	86.89	96.18	96.49	85.60	82.33	81.45	81.18
M4	✓	×	✓	86.18	85.92	96.14	95.54	81.47	80.90	79.78	79.77
M5	✓	✓	×	85.81	85.46	95.77	95.16	82.53	79.41	79.28	79.52
M6 (ours)	✓	✓	✓	88.05	**89.11**	96.20	96.20	86.68	**88.85**	81.79	**82.74**
M7	→Apex	✓	✓	87.73	88.73	**97.26**	**98.48**	85.73	87.89	80.61	81.02
M8	→Full	✓	✓	**88.26**	88.21	96.24	95.16	**88.29**	85.47	81.76	82.45
M9	→Random	✓	✓	87.89	87.87	95.42	95.45	86.36	82.91	**82.09**	82.62
M10	→Uniform	✓	✓	86.64	86.92	97.21	97.82	83.34	81.84	79.13	79.70

Apex*: Using a single onset/apex motion instance. Apex: Sampling within an apex neighborhood. Full: Full sampling. Random: Random sampling. Uniform: Uniform sampling.

4.2 Comparison with State-of-the-art Methods

We compared the proposed Ra-ICL with existing state-of-the-art (SOTA) methods under the CDE setting. The classification results on the composite dataset, CASME II, SAMM, and SMIC-HS are reported. As shown in Table 1, both UF1 and UAR of our framework on the composite dataset are higher than 88.00%, surpassing the second-best method by 2.02% in UF1 and 2.23% in UAR. Notably, on the SAMM, our method outperforms the second-best method by 5.37% in UF1 and 6.25% in UAR. Ra-ICL also achieves the best performance on CASME II and SMIC-HS datasets. Table 5 presents classification results on the CAS(ME)^3 of Ra-ICL with SOTA methods. Ra-ICL achieves the best performance in all evaluation settings, demonstrating substantial improvements compared to previous approaches. It is worth mentioning that Ra-ICL does not use any apex annotations.

We attribute the superiority of Ra-ICL to its diverse motion representations and the effective exploitation of this diversity by IRC and MRD. Although previous methods adopted well-designed classification models, their performance was still restricted by the amount of onset/apex pairs. MIR represents the ME sequence by diverse motion instances to achieve effective utilization of ME data, providing enough motion cues for subsequent classification models. With the ability to capture weaker motion information, IRC and MRD learn more robust features from diverse motion cues.

4.3 Ablation Study

To evaluate the contribution of MIR, IRC and MRD, we conducted the ablation study under the CDE setting. Table 3 quantitatively demonstrates the contributions of each design compared to the method M6 (ours) with all designs.

Multiple Instances Representation. M1 utilizes a single onset/apex instance to represent the entire ME sequence, while M2 is based on MIR with middle sampling. M3 is similar to M1 but with IRC and MRD. The improvement from M1 to M2 and M3 to M6 demonstrates the superiority of MIR, indicating that the diversity of motion cues is more important than the intensity for classification.

We also conducted experiments for different sampling strategies of MIR from M7 to M10. M7 samples 16 frames from a window centered on the apex frame. M8 samples all frames within the ME sequence. M9 and M10 perform random sampling and uniform sampling with 16 frames, respectively. M6, M7 and M8 exhibit comparable performance, while M6 avoids using apex frames as M7 and reduces the computational cost of optical flow as M8. Compared to M6, M7 employs a relatively fixed sampling range, resulting in weaker motion diversity, and thus does not outperform M6. Although M8 provides greater motion diversity, it simultaneously introduces additional noise that may obscure the perception of subtle movements. M9 and M10 also achieve competitive results, indicating that MIR with randorm or uniform sampling also carries diverse motion cues.

Instance Region Consistency Module. From M2 and M5, we find that IRC extracts effective subtle motion cues from MIR. In addition, M4 relies solely on MRD to discover meaningful activation regions in a self-supervised manner, which lacks supervision from ground-truth labels as with M6.

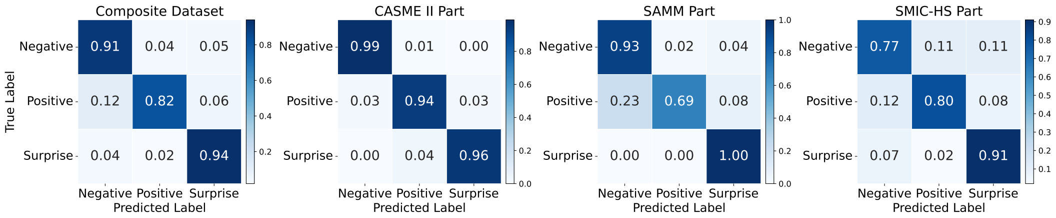

Figure 4: The confusion matrices under the CDE setting.

Multi-Region Discovery Module. The comparison between M2 and M4 indicates the ability of MRD to discover meaningful motion cues. Meanwhile, the improvement from M5 to M6 shows that MRD is helpful in expanding the attention of the model to encompass more subtle motion patterns.

4.4 Visualization

Visualization of Confusion Matrices. Figure 4 illustrates the confusion matrices under the CDE setting. We observe that the error primarily comes from misclassifying positive as negative. This phenomenon may stem from the bias of the model due to the largest amount of negative data.

Visualization of Attention Heatmaps. We conducted visualizations of attention heatmaps on a ME sequence using Grad-CAM (Selvaraju et al., 2017), as shown in Figure 5. Each row corresponds to a motion instance that shares three consistent activation regions: A, B, and C. Column (a) shows that the intensity of region C increases from row 1 to row 3, while the intensity of regions A and B keeps stable across three rows.

In column (b), attention heatmaps on three motion instances cover different activation regions. As the intensity of region C increases from row 1 to row 3, the attention heatmaps gradually overfit to region C. In column (c), attention heatmaps on three instances focus on the consistent region B. This comparison indicates that IRC effectively enforces visual attention consistency on different motion instances within the same instance set.

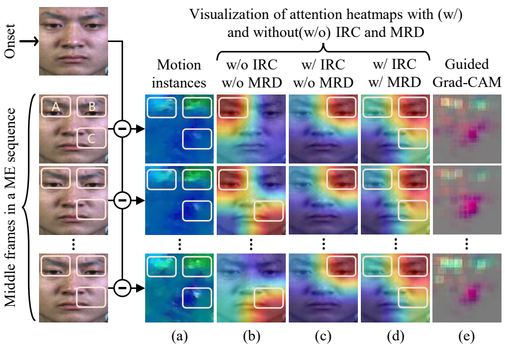
Visualization of attention heatmaps with (w/) and without(w/o) IRC and MRD
Onset
Middle frames in a ME sequence
Motion instances
w/o IRC w/o MRD
w/ IRC w/o MRD
w/ IRC w/ MRD
Guided Grad-CAM
A
B
C
(a)
(b)
(c)
(d)
(e)

Figure 5: Visualization of attention heatmaps.

Although IRC remains attention on similar regions across different instances in column (c), regions A and C are not recognized. Consequently, column (d) combines MRD into the model to discover more meaningful regions. We observe that the model is guided to allocate more attention on regions A and C, while keeping most attention on region B.

To further visualize precise pixel-level activation regions that contribute to classification, we fuse Guided Backpropagation (GB) (Springenberg et al., 2014) and Grad-CAM via point-wise multiplication to generate Guided Grad-CAM (Selvaraju et al., 2017). As shown in column (e), pixels in regions A, B, and C contribute to the classification together. Appendix A.3 provides more visualizations of confusion matrices and attention heatmaps.

5 Conclusion

In this paper, we rethought the necessity of apex annotations and proposed an apex-free framework Ra-ICL for MER. MIR advanced the motion feature of MEs by using an instance set instead of a single motion instance. Based on MIR, IRC leveraged spatial consistency across motion instances to capture effective motion cues. Meanwhile, MRD further expanded the attention on more subtle activation regions that are easily neglected. Extensive experiments on four ME datasets demonstrated the superiority of Ra-ICL. In the future, the effectiveness of MIR deserves further investigation to promote practical applications of MER models.

REFERENCES

Xianye Ben, Yi Ren, Junping Zhang, Su-Jing Wang, Kidiyo Kpalma, Weixiao Meng, and Yong-Jin Liu. Video-based facial micro-expression analysis: A survey of datasets, features and algorithms. *IEEE transactions on pattern analysis and machine intelligence*, 44(9):5826–5846, 2021.

Wenhao Cai, Junli Zhao, Ran Yi, Minjing Yu, Fuqing Duan, Zhenkuan Pan, and Yong-Jin Liu. Mfdan: Multi-level flow-driven attention network for micro-expression recognition. *IEEE Transactions on Circuits and Systems for Video Technology*, 2024.

Mathilde Caron, Ishan Misra, Julien Mairal, Priya Goyal, Piotr Bojanowski, and Armand Joulin. Unsupervised learning of visual features by contrasting cluster assignments. *Advances in neural information processing systems*, 33:9912–9924, 2020.

Bowen Cheng, Alex Schwing, and Alexander Kirillov. Per-pixel classification is not all you need for semantic segmentation. *Advances in neural information processing systems*, 34:17864–17875, 2021.

Adrian K Davison, Cliff Lansley, Nicholas Costen, Kevin Tan, and Moi Hoon Yap. Samm: A spontaneous micro-facial movement dataset. *IEEE transactions on affective computing*, 9(1): 116–129, 2016.

Alexey Dosovitskiy, Lucas Beyer, Alexander Kolesnikov, Dirk Weissenborn, Xiaohua Zhai, Thomas Unterthiner, Mostafa Dehghani, Matthias Minderer, Georg Heigold, Sylvain Gelly, et al. An image is worth 16x16 words: Transformers for image recognition at scale. *arXiv preprint arXiv:2010.11929*, 2020.

Jennifer Endres and Anita Laidlaw. Micro-expression recognition training in medical students: a pilot study. *BMC medical education*, 9(1):47, 2009.

Xinqi Fan, Xueli Chen, Mingjie Jiang, Ali Raza Shahid, and Hong Yan. Selfme: Self-supervised motion learning for micro-expression recognition. In *Proceedings of the IEEE/CVF conference on computer vision and pattern recognition*, pp. 13834–13843, 2023.

Yee Siang Gan, Sze-Teng Liong, Wei-Chuen Yau, Yen-Chang Huang, and Lit-Ken Tan. Off-apexnet on micro-expression recognition system. *Signal Processing: Image Communication*, 74:129–139, 2019.

Zheng Gao and Ioannis Patras. Self-supervised facial representation learning with facial region awareness. In *Proceedings of the IEEE/CVF Conference on Computer Vision and Pattern Recognition*, pp. 2081–2092, 2024.

Jean-Bastien Grill, Florian Strub, Florent Altché, Corentin Tallec, Pierre Richemond, Elena Buchatskaya, Carl Doersch, Bernardo Avila Pires, Zhaohan Guo, Mohammad Gheshlaghi Azar, et al. Bootstrap your own latent-a new approach to self-supervised learning. *Advances in neural information processing systems*, 33:21271–21284, 2020.

Hao Guo, Kang Zheng, Xiaochuan Fan, Hongkai Yu, and Song Wang. Visual attention consistency under image transforms for multi-label image classification. In *Proceedings of the IEEE/CVF conference on computer vision and pattern recognition*, pp. 729–739, 2019.

Kaiming He, Xiangyu Zhang, Shaoqing Ren, and Jian Sun. Deep residual learning for image recognition. In *Proceedings of the IEEE conference on computer vision and pattern recognition*, pp. 770–778, 2016.

Jingting Li, Zizhao Dong, Shaoyuan Lu, Su-Jing Wang, Wen-Jing Yan, Yinhuan Ma, Ye Liu, Changbing Huang, and Xiaolan Fu. Cas (me) 3: A third generation facial spontaneous micro-expression database with depth information and high ecological validity. *IEEE Transactions on Pattern Analysis and Machine Intelligence*, 45(3):2782–2800, 2022.

Jingting Li, Haoliang Zhou, Yu Qian, Zizhao Dong, and Su-Jing Wang. Micro-expression recognition using dual-view self-supervised contrastive learning with intensity perception. *Neurocomputing*, 619:129142, 2025.

Xiaobai Li, Tomas Pfister, Xiaohua Huang, Guoying Zhao, and Matti Pietikäinen. A spontaneous micro-expression database: Inducement, collection and baseline. In *2013 10th IEEE International Conference and Workshops on Automatic face and gesture recognition (fg)*, pp. 1–6. IEEE, 2013.

Xiaobai Li, Xiaopeng Hong, Antti Moilanen, Xiaohua Huang, Tomas Pfister, Guoying Zhao, and Matti Pietikäinen. Towards reading hidden emotions: A comparative study of spontaneous micro-expression spotting and recognition methods. *IEEE transactions on affective computing*, 9(4): 563–577, 2017.

Sze-Teng Liong, John See, KokSheik Wong, and Raphael C-W Phan. Less is more: Micro-expression recognition from video using apex frame. *Signal Processing: Image Communication*, 62:82–92, 2018.

Sze-Teng Liong, Y. S. Gan, John See, Huai-Qian Khor, and Yen-Chang Huang. Shallow triple stream three-dimensional cnn (ststnet) for micro-expression recognition. In *2019 14th IEEE International Conference on Automatic Face Gesture Recognition (FG 2019)*, pp. 1–5, 2019. doi: 10.1109/FG.2019.8756567.

Yong-Jin Liu, Jin-Kai Zhang, Wen-Jing Yan, Su-Jing Wang, Guoying Zhao, and Xiaolan Fu. A main directional mean optical flow feature for spontaneous micro-expression recognition. *IEEE Transactions on Affective Computing*, 7(4):299–310, 2015.

Chuang Ma, Shaokai Zhao, Yu Pei, Liang Xie, Erwei Yin, and Ye Yan. A multi-prior fusion network for video-based micro-expression recognition. In *ICASSP 2025-2025 IEEE International Conference on Acoustics, Speech and Signal Processing (ICASSP)*, pp. 1–5. IEEE, 2025.

Arsha Nagrani, Joon Son Chung, and Andrew Zisserman. Voxceleb: a large-scale speaker identification dataset. *arXiv preprint arXiv:1706.08612*, 2017.

Xuan-Bac Nguyen, Chi Nhan Duong, Xin Li, Susan Gauch, Han-Seok Seo, and Khoa Luu. Micron-bert: Bert-based facial micro-expression recognition. In *Proceedings of the ieee/cvf conference on computer vision and pattern recognition*, pp. 1482–1492, 2023.

Maureen O'sullivan, Mark G Frank, Carolyn M Hurley, and Jaspreet Tiwana. Police lie detection accuracy: The effect of lie scenario. *Law and human behavior*, 33(6):530–538, 2009.

Adam Paszke, Sam Gross, Francisco Massa, Adam Lerer, James Bradbury, Gregory Chanan, Trevor Killeen, Zeming Lin, Natalia Gimelshein, Luca Antiga, et al. Pytorch: An imperative style, high-performance deep learning library. *Advances in neural information processing systems*, 32, 2019.

John See, Moi Hoon Yap, Jingting Li, Xiaopeng Hong, and Su-Jing Wang. Megc 2019–the second facial micro-expressions grand challenge. In *2019 14th IEEE International Conference on Automatic Face & Gesture Recognition (FG 2019)*, pp. 1–5. IEEE, 2019.

Ramprasaath R Selvaraju, Michael Cogswell, Abhishek Das, Ramakrishna Vedantam, Devi Parikh, and Dhruv Batra. Grad-cam: Visual explanations from deep networks via gradient-based localization. In *Proceedings of the IEEE international conference on computer vision*, pp. 618–626, 2017.

Aliaksandr Siarohin, Stéphane Lathuilière, Sergey Tulyakov, Elisa Ricci, and Nicu Sebe. First order motion model for image animation. *Advances in neural information processing systems*, 32, 2019.

Karen Simonyan and Andrew Zisserman. Two-stream convolutional networks for action recognition in videos. *Advances in neural information processing systems*, 27, 2014.

Jost Tobias Springenberg, Alexey Dosovitskiy, Thomas Brox, and Martin Riedmiller. Striving for simplicity: The all convolutional net. *arXiv preprint arXiv:1412.6806*, 2014.

Javier Sánchez Pérez, Enric Meinhardt-Llopis, and Gabriele Facciolo. TV-L1 Optical Flow Estimation. *Image Processing On Line*, 3:137–150, 2013. `https://doi.org/10.5201/ipol.2013.26`.

Ashish Vaswani, Noam Shazeer, Niki Parmar, Jakob Uszkoreit, Llion Jones, Aidan N Gomez, Łukasz Kaiser, and Illia Polosukhin. Attention is all you need. *Advances in neural information processing systems*, 30, 2017.

Zhifeng Wang, Kaihao Zhang, Wenhan Luo, and Ramesh Sankaranarayana. Htnet for micro-expression recognition. *Neurocomputing*, 602:128196, 2024.

Yunchao Wei, Jiashi Feng, Xiaodan Liang, Ming-Ming Cheng, Yao Zhao, and Shuicheng Yan. Object region mining with adversarial erasing: A simple classification to semantic segmentation approach. In *Proceedings of the IEEE conference on computer vision and pattern recognition*, pp. 1568–1576, 2017.

Xuecheng Wu, Heli Sun, Yifan Wang, Jiayu Nie, Jie Zhang, Yabing Wang, Junxiao Xue, and Liang He. Avf-mae++: Scaling affective video facial masked autoencoders via efficient audio-visual self-supervised learning. In *Proceedings of the Computer Vision and Pattern Recognition Conference*, pp. 9142–9153, 2025.

Zhaoqiang Xia, Xiaopeng Hong, Xingyu Gao, Xiaoyi Feng, and Guoying Zhao. Spatiotemporal recurrent convolutional networks for recognizing spontaneous micro-expressions. *IEEE Transactions on Multimedia*, 22(3):626–640, 2019.

Shiting Xu, Zhiheng Zhou, and Junyuan Shang. Asymmetric adversarial-based feature disentanglement learning for cross-database micro-expression recognition. In *Proceedings of the 30th ACM international conference on multimedia*, pp. 5342–5350, 2022.

Wen-Jing Yan, Xiaobai Li, Su-Jing Wang, Guoying Zhao, Yong-Jin Liu, Yu-Hsin Chen, and Xiaolan Fu. Casme ii: An improved spontaneous micro-expression database and the baseline evaluation. *PloS one*, 9(1):e86041, 2014.

Zhijun Zhai, Jianhui Zhao, Chengjiang Long, Wenju Xu, Shuangjiang He, and Huijuan Zhao. Feature representation learning with adaptive displacement generation and transformer fusion for micro-expression recognition. In *Proceedings of the IEEE/CVF conference on computer vision and pattern recognition*, pp. 22086–22095, 2023.

Bohao Zhang, Xuejiao Wang, Changbo Wang, and Gaoqi He. Dynamic stereotype theory induced micro-expression recognition with oriented deformation. In *Proceedings of the Computer Vision and Pattern Recognition Conference*, pp. 10701–10711, 2025a.

Liangfei Zhang, Xiaopeng Hong, Ognjen Arandjelović, and Guoying Zhao. Short and long range relation based spatio-temporal transformer for micro-expression recognition. *IEEE Transactions on Affective Computing*, 13(4):1973–1985, 2022a.

Ren Zhang, Jianqin Yin, Chao Qi, Yonghao Dang, Zehao Wang, Zhicheng Zhang, and Huaping Liu. Facial 3d regional structural motion representation using lightweight point cloud networks for micro-expression recognition. *IEEE Transactions on Affective Computing*, 2025b.

Yuhang Zhang, Chengrui Wang, Xu Ling, and Weihong Deng. Learn from all: Erasing attention consistency for noisy label facial expression recognition. In *European Conference on Computer Vision*, pp. 418–434. Springer, 2022b.

Guoying Zhao and Matti Pietikainen. Dynamic texture recognition using local binary patterns with an application to facial expressions. *IEEE transactions on pattern analysis and machine intelligence*, 29(6):915–928, 2007.

Shuhuan Zhao, Shen Li, Yudong Zhang, and Shuaiqi Liu. Channel self-attention residual network: Learning micro-expression recognition features from augmented motion flow images. *IEEE Transactions on Affective Computing*, 2025.

Bolei Zhou, Aditya Khosla, Agata Lapedriza, Aude Oliva, and Antonio Torralba. Learning deep features for discriminative localization. In *Proceedings of the IEEE conference on computer vision and pattern recognition*, pp. 2921–2929, 2016.

Ling Zhou, Qirong Mao, and Luoyang Xue. Dual-inception network for cross-database micro-expression recognition. In *2019 14th IEEE international conference on automatic face & gesture recognition (FG 2019)*, pp. 1–5. IEEE, 2019.

Ling Zhou, Qirong Mao, Xiaohua Huang, Feifei Zhang, and Zhihong Zhang. Feature refinement: An expression-specific feature learning and fusion method for micro-expression recognition. *Pattern Recognition*, 122:108275, 2022.

A Appendix

A.1 More Experimental Details

A.1.1 Datasets

We conducted experiments on four public ME datasets: CASME II (Yan et al., 2014), SAMM (Davison et al., 2016), SMIC-HS (Li et al., 2013) and CAS(ME)^3 (Li et al., 2022).

CASME II provides 255 samples collected from 26 subjects. These samples are classified into five categories, including Happiness, Repression, Surprise, Disgust, and Others. Videos are at 200 frames per second (fps).

SAMM contains 159 samples from 32 participants with eight categories, including Happiness, Surprise, Anger, Disgust, Sadness, Fear, Contempt, and Others. The frame rate is 200 fps.

SMIC-HS consists of 164 samples from 16 subjects classified into three categories: Positive, Negative, and Surprise. The samples are captured at 100 fps.

CAS(ME)^3 part A comprises 860 samples from 100 subjects. These samples are classified into seven categories: Happiness, Anger, Fear, Disgust, Surprise, Sadness, and Others. The frame rate is set at 30 fps.

A.1.2 Determination of the number N for MIR

For MIR with middle sampling, we divide the ME sequence into three segments of equal length: the initial segment, the middle segment, and the end segment. The middle segment corresponds to the sampling window. Therefore, the number of sampled frames N (i.e., the length of the middle segment) can vary across different ME sequences. If the length of a ME sequence is T, then the number N can be obtained by:

$$N = \frac{T}{3}. \tag{16}$$

To simplify the construction of instance sets, we set a unified value of N for all sequences based on the frame rate prior of datasets. Specifically, the duration of a ME sequence is typically less than 0.5 seconds. Denote the frame rate as f, the number N should satisfy the equation 17:

$$N \leq \frac{1}{3} \cdot 0.5 \cdot f = \frac{f}{6} \tag{17}$$

Under the CDE setting, the lowest frame rate is 100 fps from the SMIC-HS dataset. Therefore, setting N to 16 is a reasonable choice, as it ensures motion diversity while satisfying the requirement of the equation 17. For the CAS(ME)^3 dataset, although its frame rate is 30 fps, sequence lengths vary from just a few frames to over 100 frames, which do not strictly adhere to the constraint of less than 0.5 seconds. For consistency, we also set N to 16 on the CAS(ME)^3 dataset. For all datasets, we apply full sampling (i.e., all frames are used) on sequences containing fewer than 16 frames.

A.1.3 Experimental Configurations

All experiments were performed on a high-performance computer with 16 CPU cores, 1 NVIDIA 3090 Ti GPU card, and 32 GB memory. Both online and target networks are not pretrained. Their parameters are randomly initialized. For inference, we choose the middle instance in an instance set as input to the online network. The reason for selecting middle instances is similar to that of middle sampling: to avoid using instances with excessively low motion intensity for inference.

A.1.4 Evaluation Protocols

For CASME II, SAMM and SMIC-HS, we combine them into a composite dataset under the CDE setting proposed by the MEGC2019 challenge (See et al., 2019) to ensure a fair comparison. This

Table 4: Details of three datasets under the CDE setting.

Category	CASME II	SAMM	SMIC-HS	Full
Negative	88	92	70	250
Positive	32	26	51	109
Surprise	25	15	43	83
Total	145	133	164	442

Table 5: Details of 3-class, 4-class and 7-class evaluation on CAS(ME)^3.

3-class		4-class		7-class	
Negative	438	Negative	438	Anger	55
				Fear	82
				Disgust	245
				Sadness	56
Positive	49	Positive	49	Happiness	49
Surprise	183	Surprise	183	Surprise	183
\	\	Others	131	Others	131
All	670	All	801	All	801

challenge aims to create a more realistic emotion recognition scenario by expanding the diversity of data to support data-driven deep learning. To reduce ambiguity from different stimuli and settings, emotion categories are simplified into three categories as those in SMIC-HS: **Negative** {“Repression”, “Disgust”, “Anger”, “Sadness”, “Fear”, “Contempt”}, **Positive** {“Happiness”} and **Surprise** {“Surprise”}. Samples of “Others” are excluded. The final distribution with a total of 442 samples under the CDE setting is shown in Table 4. These 442 samples belong to 68 subjects. CASME II, SAMM and SMIC-HS contain 24, 28 and 16 subjects, respectively. Therefore, the Leave-one-subject-out (LOSO) cross-validation should be repeated 68 times. In each evaluation, each subject serves as the testing set, while the remaining subjects form the training set.

For the CAS(ME)^3 dataset, the evaluation is conducted individually for a fair comparison. 3-class, 4-class and 7-class evaluation with LOSO are reported following previous works (Li et al., 2022; Nguyen et al., 2023). The officially provided labels contain seven categories: Happiness, Anger, Fear, Disgust, Surprise, Sadness, and Others. We conducted a 7-class evaluation on these seven categories. Similarly, we can simplify the seven categories into four categories: Negative, Positive, Surprise, and Others. These four categories can be used in 4-class evaluation. Furthermore, samples labeled as “Others” can be omitted to conduct a 3-class evaluation. Details of 3-class, 4-class and 7-class evaluation are shown in Table 5. Some samples with annotation errors are excluded.

A.1.5 Metrics

To provide a more balanced judgement on all classes, we use Unweighted F1-score (UF1) and Unweighted Average Recall (UAR) instead of the standard Accuracy (Acc). The UF1 is defined as:

$$\mathrm{F1}_c = \frac{2 \cdot \mathrm{TP}_c}{2 \cdot \mathrm{TP}_c + \mathrm{FP}_c + \mathrm{FN}_c} \tag{18}$$

$$\mathrm{UF1} = \frac{1}{C} \sum_c \mathrm{F1}_c \tag{19}$$

where TP_c, FP_c and FN_c are true positives, false positives, and false negatives for class c, respectively. C is the total number of classes. The UAR is defined as:

$$\mathrm{UAR} = \frac{1}{C} \sum_c \frac{\mathrm{TP}_c}{n_c} \tag{20}$$

where n_c is the number of samples of the c-th class.

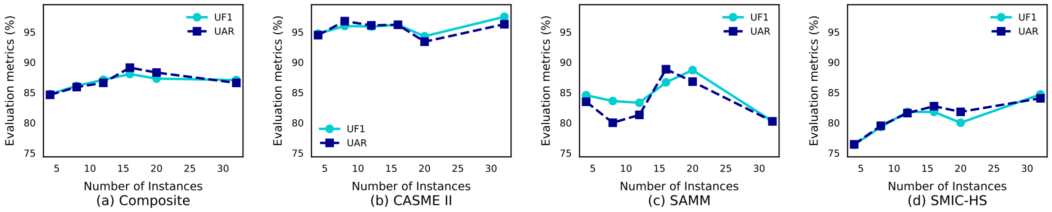

(a) Composite (b) CASME II (c) SAMM (d) SMIC-HS

Figure 6: Hyper-parameter analysis on the number of instances under the CDE setting.

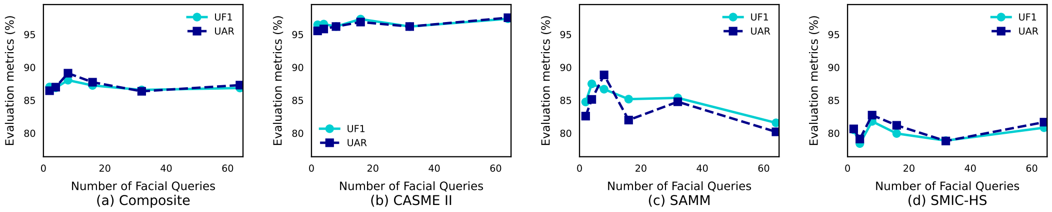

(a) Composite (b) CASME II (c) SAMM (d) SMIC-HS

Figure 7: Hyper-parameter analysis on the number of facial queries under the CDE setting.

A.2 Hyper-Parameter Analysis

A.2.1 Influence of Different Numbers of Instances

We conduct experiments on different numbers of motion instances. Considering that MEs are usually recorded below or equal to 200 fps, and ME sequences generally last less than 0.5 seconds, we selected 4, 8, 12, 16, 20, and 32 as different number of instances for a sequence. When the number of instances is fewer than 16, the middle sampling window is compressed inward. When it exceeds 16, the window expands outward toward both ends of the sequence. If the required number of instances exceeds the sequence length, full sampling is performed.

As shown in Figure 6, the model achieves the best performance when the number of instances is 16. When the number of instances is less than 16, the motion information becomes insufficiently diverse, resulting in less robust features. In contrast, when the number of instances is larger than 16, the model exhibits a slight decline in overall performance. Although increased instances provide greater motion diversity, they simultaneously introduce additional noise that may obscure the ability of the model to perceive subtle micro-movements. Therefore, it is not appropriate to increase the number of instances excessively, as it necessitates a careful trade-off between motion diversity and noise introduction.

A.2.2 Influence of Different Numbers of Facial Queries

MRD is enforced to discover distinct facial regions by different facial queries. Figure 7 shows the effect of different numbers of facial queries. The optimal number of facial queries is 8. If the number of facial queries is smaller, the model is at risk of failing to identify complete and meaningful facial activation regions. Conversely, if the number of facial queries is excessively large, the model may overfit to non-discriminative motion noise. This would impair its discriminative capability for critical ME features.

A.2.3 Influence of Different Loss Weights

The overall objective contains three loss weights $\lambda_1, \lambda_2, \lambda_3$ for the balance of classification, IRC, and MRD, respectively. To show the influence of these three loss weights on performance, we evaluated them from 0.1 to 2 under the CDE setting.

Figure 8 shows that the optimal λ_1 is around 0.5. When λ_1 approaches zero, the guidance from ground-truth labels reduces, resulting in a decrease in performance. As λ_1 increases, classification takes precedence, compromising the effectiveness of both IRC and MRD modules and leading to degraded performance.

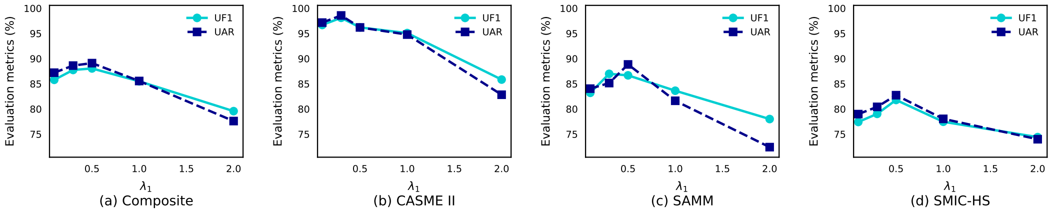

(a) Composite (b) CASME II (c) SAMM (d) SMIC-HS

Figure 8: Hyper-parameter analysis on λ_1 under the CDE setting.

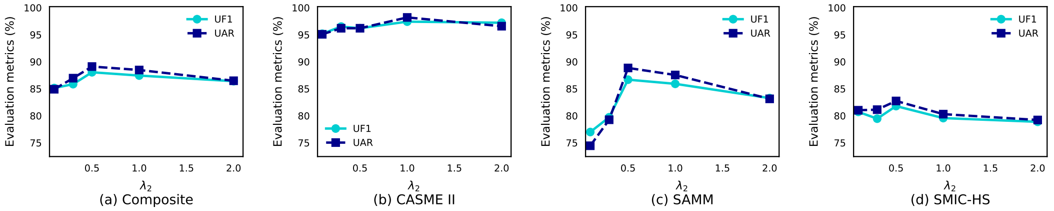

(a) Composite (b) CASME II (c) SAMM (d) SMIC-HS

Figure 9: Hyper-parameter analysis on λ_2 under the CDE setting.

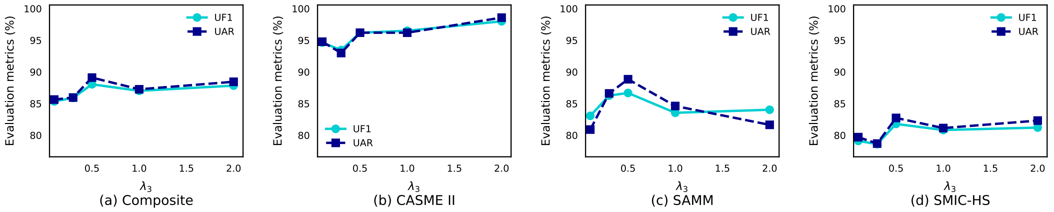

(a) Composite (b) CASME II (c) SAMM (d) SMIC-HS

Figure 10: Hyper-parameter analysis on λ_3 under the CDE setting.

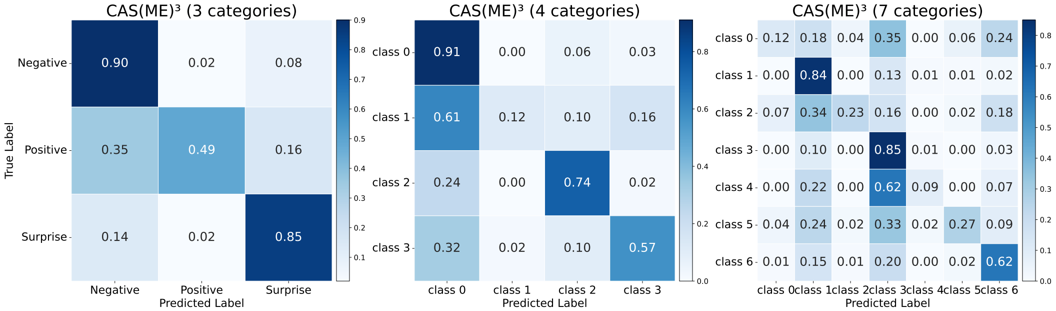

Figure 11: The confusion matrices on the CAS(ME)^3 dataset (From left to right: 3-class evaluation, 4-class evaluation, 7-class evaluation). For the 4-class evaluation, labels {0, 1, 2, 3} correspond to {negative, positive, surprise, others}. For the 7-class evaluation, labels {0, 1, 2, 3, 4, 5, 6} correspond to {happiness, surprise, sadness, disgust, fear, anger, others}.

Figure 9 demonstrates that the optimal value of λ_2 is approximately 0.5. The performance first increases along λ_2 and then decreases. If λ_2 is too small, the model will overfit to certain activation regions. If λ_2 is set larger than 0.5, the performance decreases slightly since the attention consistency loss outweighs the classification loss.

Figure 10 illustrates that the model achieves the best performance when λ_3 is equal to 0.5. When $\lambda_3 < 0.5$, the MRD module does not sufficiently constrain the model to identify more meaningful regions. When $\lambda_3 > 0.5$, it disrupts the learning process of both classification and IRC.

A.3 Visualization

A.3.1 Visualization of Confusion Matrices

Figure 11 shows the confusion matrices of Ra-ICL on the CAS(ME)^3 dataset. For the confusion matrix with 3 categories, we find that the model performs better on the negative and surprise classes but worse on the positive class. In the confusion matrix with four categories, we also observed that the positive class performed poorly. This may stem from the fewest samples of the positive class in the dataset, leading to biased model predictions. Meanwhile, the result shown in the confusion matrix with seven categories demonstrates that the model performs better in the surprise, disgust, and others classes. The three classes correspond to the three classes with the highest number of samples in the CAS(ME)^3 dataset.

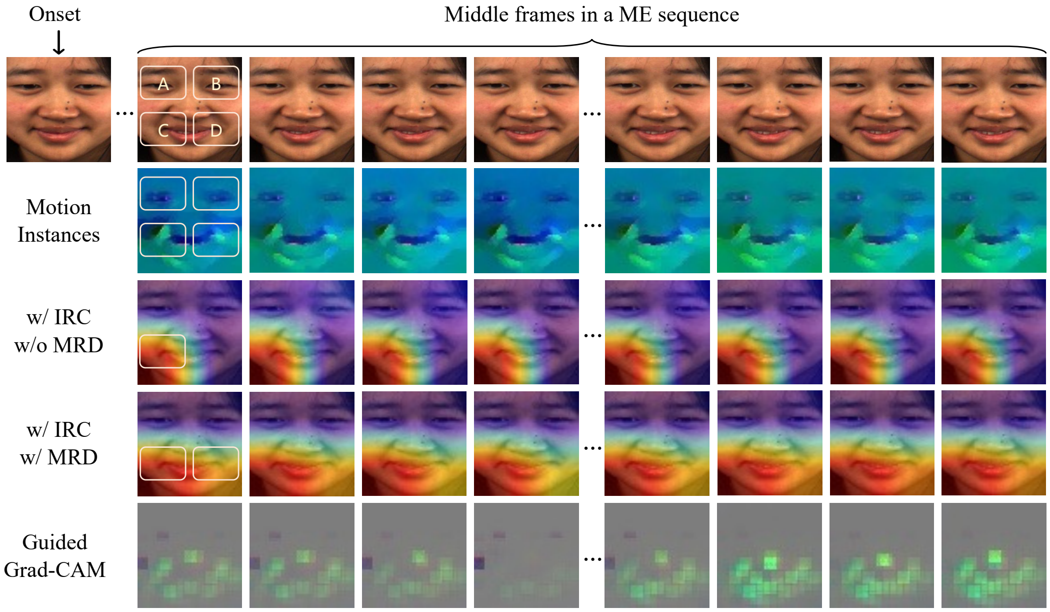

Figure 12: The visualization of attention heatmaps. The first row: RGB frames of a ME sequence. The second row: Motion instances. The third row: Attention heatmaps of the model with (w/) the IRC module but without (w/o) the MRD module. The fourth row: Attention heatmaps of the model with both IRC and MRD modules. The fifth row: Guided Grad-CAM of each motion instance.

A.3.2 Visualization of Attention Heatmaps

We conducted visualizations of attention heatmaps on a ME sequence using Grad-CAM (Selvaraju et al., 2017). Figure 12 shows a ME sequence with four facial activation regions: A, B, C, and D. The third row illustrates the attention regions of the model when equipped with the IRC module but without the MRD module. It is evident that the model consistently focuses on region C across all motion instances, indicating that IRC effectively enforces visual attention consistency for all instances within an instance set. However, without MRD, the attention region fails to cover region D. The fourth row represents the attention regions when both IRC and MRD modules are implemented. We observe that the model not only maintains consistent attention regions across all samples in the set but also expands its focus to the region D. Note that A and B indicate eye movements, which should be considered noise in this sample. In both the third and fourth rows, the attention of the model avoids regions A and B. This demonstrates the capability of the model to effectively distinguish between noise and subtle motions that contribute to classification. The fifth row presents the Guided Grad-CAM (Selvaraju et al., 2017; Springenberg et al., 2014) for each motion instance. It is illustrated that pixels in regions C and D are critical for classification.

B The Use of Large Language Models

We used Large Language Models (LLMs) solely to aid and polish the writing of this paper. LLMs were not involved in the generation of research ideas, conceptualization, research design, or experimental design. The authors take full responsibility for all content presented in this manuscript, including any content generated or polished with the assistance of LLMs.